Heavily Doped Si Nanocrystals Formed in P-(SiO/SiO 2) Multilayers: A Promising Route for Si-Based Infrared Plasmonics

Alix Valdenaire, Alaa Eldin Giba, Mathieu Stoffel, Xavier Devaux, Loïc Foussat, Jean-Marie Poumirol, Caroline Bonafos, Sonia Guehairia, Rémi Demoulin, Etienne Talbot, et al.

Heavily Doped Si Nanocrystals Formed in P-(SiO/SiO_2) Multilayers: a Promising Route for Si-Based Infrared Plasmonics

Alix Valdenaire,[1] Alaa Eldin Giba,[1,2] Mathieu Stoffel,[1,*] Xavier Devaux,[1] Loïc Foussat,[3] Jean-Marie Poumirol,[3] Caroline Bonafos,[3] Sonia Guehairia,[4] Rémi Demoulin,[4] Etienne Talbot,[4] Michel Vergnat,[1] Hervé Rinnert[1,*]

[1]*Université de Lorraine, CNRS, Institut Jean Lamour, F-54000 Nancy, France*
[2]*National Institute of Laser Enhanced Sciences, Cairo University, Giza 12613, Egypt*
[3]*CEMES-CNRS, Université de Toulouse, CNRS, 31055 Toulouse*
[4]*Normandie Univ., UNIROUEN, INSA Rouen, CNRS, Groupe de Physique des Matériaux, 76000 Rouen, France*

Abstract

As building blocks of multifunctional materials involving coupling at the nanoscale, highly doped semiconductor nanocrystals are of great interest for potential applications in nanophotonics. In this work, we investigate the plasmonic properties of highly doped Si nanocrystals embedded in a silica matrix. These materials are obtained by evaporation of heavily Phosphorus-doped SiO/SiO_2 multilayers in a ultrahigh vacuum chamber followed by rapid thermal annealing. For P contents between 0.7 and 1.9 at%, structural investigations at the nanoscale give clear evidence that P atoms are mainly located in the core of Si nanocrystals with concentrations reaching up to 10 at%, i.e. well beyond the solid solubility limit of P in bulk Si. Alloying and formation of SiP nanoparticles is observed for P contents exceeding 4 at% in the multilayer. Infrared absorption measurements give evidence of a localized surface plasmon resonance located in the 3 to 6 µm range. A core-shell structure was used to model Si nanocrystals embedded in a silica matrix. Based on the Mie theory and the Drude model, both the mobility and the free charge carrier density were extracted from the simulation, with values reaching 27 $cm^2V^{-1}s^{-1}$ and 2.3×10^{20} cm^{-3}, respectively. This results in a dopant activation rate of about 8 %.

Keywords: Si nanocrystals, phosphorus, hyperdoping, LSPR, infrared absorption spectroscopy

*Corresponding authors: mathieu.stoffel@univ-lorraine.fr; herve.rinnert@univ-lorraine.fr

1. INTRODUCTION

Localized surface plasmon resonance (LSPR) corresponds to the collective oscillations of free charge carriers confined in a nanoparticle driven by an electromagnetic field. Many different plasmonic materials have been considered till now in the literature. Among them, noble metals such as Au or Ag nanostructures have first gained a significant interest. Indeed, their large free charge carrier concentration (10^{22} -10^{23} cm^{-3}) is known to lead to a plasmon resonance in the visible spectral range. The coupling between the plasmon and the electric field of the incoming light leads to a significant enhancement of the absorption or fluorescence which has been exploited for various applications such as detection of single molecules[1] and more generally label-free biosensing[2]. However, due to the fact that Au and Ag-based nanostructures are not compatible with the Complementary Metal Oxide Semiconductor (CMOS) technology, and with the aim to extent the spectral range in the infrared range with nanometer-sized structures, alternative materials like heavily doped quantum dots and metal oxide nanocrystals have been explored[3,4]. By reducing the charge carrier concentration, the plasmon resonance can be possibly shifted to the near and mid-infrared which may further extend the range of potential applications[5]. Many different materials such as silicides[6], germanides[7] but also conducting oxides and nitrides as well as transition metal nitrides[8-10] were shown to exhibit a strong potential for near-infrared plasmonics. Alternatively, doped semiconductor nanocrystals may also be of great interest[11]. Several studies have concerned semiconductor nanocrystals such as $Cu_{2-x}S$, $Cu_{2-x}Se$, $Cu_{2-x}Te$[12-14] but also ZnO[15] and ITO[16]. Due to their low cost, their compatibility with the CMOS technology, their ease of fabrication and their non-toxicity, Si nanocrystals (Si-NCs) appear particularly promising. Although some theoretical works suggested that insertion of dopants at the nanoscale is not favored by thermodynamics[17], several authors have nevertheless shown that Si-NCs can contain P atoms or B atoms[18-20]. Moreover, hyperdoping has emerged as a possible route to generate LSPR in Si-NCs. Using tight binding calculations,

Pi and Delerue[21] have investigated the optical response of hyperdoped Si-NCs. For Si-NCs having sizes of about 4 nm, a LSPR can be possibly obtained when the nanocrystals contain more than 10 P atoms. Rowe et al.[22] gave the first experimental evidence of a tunable mid-infrared LSPR in free-standing phosphorus doped Si-NCs. The latter were obtained by a nonthermal plasma method and P was supplied by PH_3 gas. The plasmonic properties of both heavily phosphorus and boron doped Si-NCs prepared by non-thermal plasma were further studied, reporting different behaviors depending on whether the Si-NCs are doped with boron or phosphorus[23-25]. Poumirol et al.[26] used a combination of e-beam lithography and reactive ion etching to fabricate ordered arrays of P-hyperdoped Si nanodisks on a Silicon-On-Insulator substrate. By adjusting the free carrier concentration, the tunability of the LSPR was demonstrated in a large spectral window ranging from 2 μm to 5 μm. In addition, numerical simulations based on the Green Dyadic Method (GDM) were used to calculate the extinction efficiency of a single Si-nanodisk, which is found to be in good agreement with the experimental LSPR. The reflectance was further studied as a function of the spacing between nanodisks. Majorel at al.[27] used the same kind of simulations to investigate doped silicon nanostructures having an arbitrary shape. Both the extinction coefficient as well as the electromagnetic field in and around any kind of nanostructure can be calculated precisely thus enabling the control of light in and around tiny structures. Very recently, Zhang et al.[28] reported the observation of LSPR in a single layer of hyperdoped Si-NCs, with characteristic sizes lower than 6 nm, prepared by low energy ion implantation in a silica matrix and rapid thermal annealing. They demonstrated than only few electrons in a nanocrystal can give rise to LSPR. Till now, only the plasmonic properties of heavily doped, free-standing Si-NCs as well as single layers of hyperdoped Si-NCs embedded in a silica matrix have been considered. In the case of free-standing Si-NCs, the plasmonic properties turned out to be sensitive to oxidation[23] and more generally to the modification of the chemical environment[24], which could be detrimental

to applications. Moreover, in the case of a single layer of hyperdoped Si-NCs embedded in a silica matrix, the absorption remains weak[28].

In this paper, we report on a tunable LSPR from heavily P-doped Si-NCs formed in P-(SiO/SiO_2) multilayers. The multilayer approach has been successfully applied to achieve highly luminescent and size-controlled Si-NCs[29,30]. To date, there is no report in the literature concerning heavily doped Si-NCs showing LSPR obtained using the well-known multilayer architecture. This approach offers several advantages: firstly, thanks the SiO_2 barrier layers, the size of the Si-NCs can be controlled by the SiO layer thickness, and secondly, several layers of heavily doped Si-NCs can contribute to the LSPR thereby improving the signal. In a first part, the structure and the local chemical composition of the multilayers are determined by combining atom probe tomography (APT), advanced scanning transmission electron microscopy (STEM) and electron energy loss spectroscopy (EELS) mapping at the atomic scale. In a second part, the absorption properties measured by Fourier-transform infrared absorption spectroscopy (FTIR) are presented. Simulations based on the theory of Mie and assuming a core-shell model were able to reproduce correctly both the vibrational and the electronic contributions to the absorption spectra. They allow us to determine both the mobility and the density of the charge carriers from which the activation rate of the dopants inserted into Si-NCs were deduced.

2. EXPERIMENTAL SECTION

P-doped SiO/SiO_2 multilayers were grown by alternating evaporation of both SiO and SiO_2 provided by e-beam guns on Si(100) substrates held at room temperature. The deposition rates of SiO and SiO_2 were controlled by a quartz microbalance and fixed at 0.1 nm/s. The SiO/SiO_2 layer thicknesses were kept at 10 nm and 6 nm, respectively. The multilayers consist of 20 doublets of SiO/SiO_2 with a total nominal thickness of 320 nm (scheme 1). P atoms were supplied by a GaP decomposition source[31] held at a constant temperature during the whole

deposition process thus leading to incorporation of P atoms in both SiO and SiO_2 layers. As-deposited multilayers were amorphous. The samples were then post-grown annealed in a rapid thermal annealing furnace at various temperatures for 5 or 15 minutes under N_2 flow (200 sccm) to destabilize the SiO layer and to form Si-NCs (scheme 1). The microstructural properties were investigated by energy filtered transmission electron microscopy (EFTEM), STEM, STEM-EELS and STEM energy dispersive spectroscopy (EDS). Electron microscopy and the associated spectroscopies were carried out on a probe corrected JEOL ARM 200 F equipped with a cold-field emission gun. EELS spectrum images (SI) were recorded with a GATAN GIF quantum ER filter. To avoid sample destruction caused by the electron beam, all experiments were carried out at 80 kV with a maximal probe current of about 50 pA for EELS spectrum images and EDS mapping. Two EELS-SI images were simultaneously recorded for the low loss part containing the zero loss and for the core-loss which allows advanced data post-processing like energy drift and multiple scattering corrections. The spectra were recorded with an electron beam having a half convergence angle of 24 mrad and a half collection angle of 56 mrad with an energy dispersion of 0.05 eV per channel and a pixel time of 0.005 s. SI were recorded with a spatial sampling of about 0.2 x 0.2 nm^3 per pixel. A multivariate statistical analysis software was used to improve the quality of the STEM-EELS data by de-noising the core-loss SI. Low loss spectra were processed by zero-loss extraction and Fourier-log deconvolution for multiple scattering corrections. To obtain chemical maps, multiple linear least square fitting was applied on Si_L and P_L signals. Due to the overlapping of both Si_L and P_L edges and to separate different chemical states of Si (Si^0 and Si^{IV}), reference spectra were recorded on pure Si, on thermal silica grown on pure Si and on SiP_2. The reference spectra were extracted from SI recorded on lamellae with the same thickness and with the same STEM and spectrometer parameters than that used for the sample under study. More detailed information on this procedure was previously published[32,33]. For STEM observations, lamellas thinned up to $t/\lambda < 0.8$ (ratio

between the thickness and the mean free path of primary electrons) were prepared by focused ion beam (FIB) using a FEI Helios Nanolab 600i dual beam microscope. During FIB operation, the multilayers were capped by a pure carbon layer prior to deposition of a Pt-C layer to protect the sample during the first steps of the lamella extraction. After FIB milling, the lamellae were stored in vacuum to prevent oxidation. Atom probe tomography (APT) was further used to investigate the structural and chemical properties at the nanoscale. The experiments were carried out using a laser assisted wide angle tomographic atom probe (LAWATAP, Cameca) using a femtosecond UV pulsed laser (λ=343 nm, 350 fs, 33 nJ). The analysis was performed in an ultra-high vacuum chamber (10^{-10} mbar) at T = 80 K. Tip shaped samples were prepared using a Thermoscientific plasma FIB Helios G4 XCe. The data treatments and the 3D reconstructions were performed by using GPM3D software. The infrared absorption spectra were obtained using a Fourier transform infrared (FTIR) absorption spectrometer. The spectra of the thin films were obtained after subtraction of the reference spectrum measured on a Si substrate. The steady state photoluminescence (PL) was excited by an arc source xenon lamp. A monochromator was used to select an excitation centered at 325 nm with a full width at half maximum of 5 nm. The signal was collected by a monochromator equipped with a 150 grooves per mm grating and measured by a cooled CCD camera operating in the visible-near infrared range. All spectra were corrected from the response of the system.

3. RESULTS AND DISCUSSION

Figure 1 shows the evolution of the chemical composition for P-doped SiO/SiO_2 multilayers grown with different temperatures of the GaP decomposition source ranging between 780°C and 860°C. The elemental concentrations were determined by energy dispersive spectroscopy measurements performed on the whole multilayer structure. The obtained values were further cross-checked by atom probe tomography. The P content in the multilayers can be simply adjusted by varying the temperature of the GaP decomposition source. The P content was thus

controlled from about 0.3 at% up to 4.1 at% when the GaP decomposition source temperature is increased from 780°C up to 860°C. Figure 2(a) shows an energy filtered transmission electron microscopy (EFTEM) image of a P-doped SiO/SiO_2 multilayer containing 1.1 at% of P annealed at 1100°C for 15 minutes. The image is obtained by selecting the silica plasmon peak at 25 eV for imaging (slit width 1 eV). The silica matrix appears in light grey while Si and PtC layer are darker. One can clearly identify a rather high density of nanoparticles almost randomly dispersed in the silica matrix. A high resolution TEM micrograph of a single nanoparticle is shown in Fig. 2(b) with a fast Fourier transform in the inset. They show that the nanoparticles are mainly single crystalline with the Si diamond-like cubic structure. The expected multilayer structure is no longer fully preserved as a result of the P-induced softening of the silica matrix, as already mentioned in a previous work[20] or by the increase of atomic diffusion induced by dopants[34]. The Si-NCs size remains however limited and almost controlled by the presence of the SiO_2 barrier layers, as shown by the histograms of the size distribution (Fig. 2(f)). For the undoped layer, the corresponding histogram shows that the average Si-nanocrystal size is close to 7 nm, which is lower than the nominal thickness of the SiO layers (i.e. 10 nm). This is due to the weak density of the SiO layer that is obtained by evaporation in ultrahigh vacuum with a substrate maintained at room temperature. The densification of the SiO layer induced by the annealing treatment leads to the formation of Si-NCs having diameters slightly lower than the nominal SiO layer thickness. For the doped multilayers, an increase of the Si-NCs size is observed up to a mean size close to 15 nm. To get further information on the local chemistry, we used STEM-EELS to map the chemical distribution of the elements at the nanoscale. Figures 2(c)-(e) show the chemical maps relative to Si^0, P and Si^{4+}, respectively. Si^0 atoms are localized in the substrate and in the nanocrystals formed in the sample. Si^{4+} atoms (corresponding to Si atoms present in SiO_2) are located in the matrix surrounding the nanocrystals. Interestingly, P atoms appear localized mainly in the nanocrystals. However, since EELS signals originate from

the volume irradiated by the electron probe, P atoms cannot be localized in the thickness of the TEM lamella and, one cannot exclude the presence of P atoms at the interface between Si-NCs and the surrounding silica matrix. To further clarify the location of P atoms, APT measurements have been performed on P-doped SiO/SiO_2 multilayers containing 0.7 and 1.1 at% of P. Figure 3 (a)-(b) shows typical slice views ($46 \times 46 \times 10$ nm^3) drawn from the 3D reconstructed volume and representing both Si atoms (in red) and P atoms (in black) for the multilayer containing 1.1 at% of P. One can clearly identify Si-NCs represented by a concentration of red spots (Fig. 3(a)). Their average size is about (6.5 ± 0.1) nm, in good agreement with the results obtained by STEM. Fig. 3(b) shows that P atoms can be found mainly inside Si-NCs to an amount of 60 % and in the surrounding silica matrix to an amount of 40 % thus confirming the preferential localization of P in Si-NCs evidenced by STEM-EELS measurements. The P content inside Si-NCs, which is determined by counting the number of P atoms in each Si-NC divided by the total number of atoms (Si+P) contained in the nanocrystal, is almost independent on the Si-NC diameter (Fig. 3(c)). For the multilayer containing 1.1 at% of P, the mean P content reaches a value of (10.3 ± 1.1) at%, i. e. well beyond the solid solubility limit of P in bulk Si (i.e. 6 x 10^{20} cm^{-3} at 1100°C). As the P content in the multilayers increases from 0.7 at% to 1.1 at%, the mean Si-NC size increases from about (5.4 ± 0.1) nm to (6.5 ± 0.1) nm, which is well explained by the enhanced Si diffusion in presence of P[20,35]. Meanwhile the P content in the Si-NCs also increases from about (5.6 ± 1.4) at% to (10.3 ± 1.1) at% at constant Si-NC size. However, despite the large P contents in the Si-NCs, alloying and formation of SiP nanoparticles is not observed.

Figure 4(a) shows a STEM-HAADF image of the P-doped SiO/SiO_2 multilayer with the largest P content considered in this study, i.e. 4.1 at%. Spherical shaped nanoparticles with typical sizes ranging between 10 nm and 50 nm can be identified. Typical EDS spectra measured either in a nanoparticle or in the surrounding matrix are shown in Fig. 4(b). In the matrix, both Si and

O are detected but no phosphorus. In the particles, one can identify a significant P_K peak originating from phosphorus atoms. A quantitative analysis yields a P content close to 50 %, thus suggesting that the large sized nanoparticles consist of SiP. For such high P content in the multilayer, Si-P alloying was already observed in annealed Si:P thin films[33].

Figure 5(a) shows the evolution of the PL spectra measured at room temperature on an undoped SiO/SiO_2 multilayer prior to and after annealing for 5 minutes at various temperatures between 950°C and 1100°C. For the as-deposited multilayer, no PL can be observed. This can be easily understood since phase separation and nanocrystal formation has not yet started. For annealing temperatures larger than 950°C, a rather broad PL band is observed centered at about 880 nm. This band, which is due to radiative recombinations between electrons and holes confined in Si-NCs, is found to increase and to redshift as the annealing temperature further increases up to 1100°C. The observed redshift can be well explained by the increase of the mean Si-NCs size and the induced decrease of the bandgap. When the annealing time increases from 5 to 15 minutes, the intensity of the PL band further increases and the position of the peak is slightly redshifted. The PL intensity increase can be related to an improved crystalline quality of the Si-NCs. In the following, we will investigate the evolution of the PL from P-doped SiO/SiO_2 multilayers. Figure 5(b) shows the PL spectra measured on both undoped and P-doped SiO/SiO_2 multilayers with the P content varying between 0.3 at% to 4.1 at% after annealing at 1100°C for 15 minutes. For the undoped multilayer, a strong PL band is observed centered at about 920 nm. For increasing P contents up to 0.3 at%, the PL band redshifts and its intensity strongly decreases. The observed redshift is well explained by the increase of the mean Si-NC size as shown by both APT and STEM measurements. For larger P contents, the fraction of P atoms located in the Si-NCs increases as evidenced by APT measurements (see fig. 3(c)). The PL intensity strongly decreases with the P content, which can be explained by the presence of P atoms in Si-NCs which act as non-radiative centers and/or by the Auger effect. For a P content

equal to 0.7 at%, a slight PL blueshift is observed which could be due to the quenching of the biggest Si-NCs which could contain a larger number of non-radiative defects. For higher P contents up to around 2 at%, the Si-NCs related PL is no longer measurable. Finally, for the largest P content investigated in this study (i.e. 4.1 at%), Si-NCs are no longer observed thus explaining the disappearance of the associated PL band.

Figure 6 (a) shows the Fourier transform infrared absorption spectrum measured on a multilayer containing 1.1 at% of P and annealed at 1100 °C during 15 min. We can identify several sharp features at 461 cm^{-1}, 816 cm^{-1} and 1085 cm^{-1} which are due to the rocking, bending and stretching mode of Si-O-Si bonds in silica, respectively[36]. In addition, we observe the presence of oscillations on the baseline which originate from interferences in the multilayers. Interferences are due to multiple reflections occurring at the multilayer/substrate and air/multilayer interfaces. Finally, a rather broad band is observed centered at about 2000 cm^{-1} which cannot be attributed to a vibrational contribution. According to its position, this band could possibly be the signature of a LSPR in P-doped Si-NCs. To clarify the origin of this band and to eliminate the contribution arising from interferences in the multilayers, we have firstly performed a simulation of the interferences based on the model developed by Swanepoel[37]. The result of the simulation is shown in Fig. 6(a) as a red solid line. To carry out the simulation of the interferences, the thickness of the layer was taken from the TEM analysis and the refractive index was modeled by the Cauchy relation. Figure 6(b) displays the Fourier-transform infrared absorption spectra for different P-doped multilayers with P contents varying between 0.3 at% and 4.1 at% after subtracting the contribution related to interferences. For the multilayer with the lowest P content (i.e. 0.3 at%), we can only identify the vibrational features related to the Si-O-Si bonds. No signal can be detected in the spectral range 1500-2000 cm^{-1}. However, for multilayers containing 0.7 at% and 1.1 at% of P, a rather broad band extending from 1500 cm^{-1} till 3700 cm^{-1} can be identified. Interestingly, this band shifts to larger wavenumbers as the P

content increases from 0.7 at% up to 1.1 at%. Considering the position of this broad band, which is in good agreement with previous results[22,26,28], and the observed blueshift induced by the increased P concentration, we can attribute this band to a LSPR in P-doped Si-NCs. Moreover, as expected in presence of free carriers in the nanocrystals, the emergence of a LSPR related band occurs concomitantly with the PL quenching. This occurs for a minimal P content in the Si-NCs slightly larger than 5 at%. When the P content further increases, the fraction of P atoms located in the Si-NCs increases thus leading to an increased free charge carrier density. As a result, the LSPR mode blueshifts as expected from the Drude's model. However, for a P content of about 1.9 at%, the observed trend does not continue but instead a redshift is observed. For such large P concentrations, an increased amount of P atoms either occupy interstitial sites or form small clusters, which does not lead to additional free charge carriers. Finally, for the highest P content considered in this study (i.e. 4.1 at%), we can only observe vibrational features. In this case, the STEM-EDS measurements clearly showed the formation of SiP nanoparticles (see fig. 4), which then explain the absence of any Si-NC related LSPR band.

To determine the free charge carrier density as well as the mobility of the free charge carriers, simulations of the infrared absorption spectra were carried out assuming a core-shell model (Fig. 7(a)). Spherical shaped Si-NCs at the core being surrounded by a SiO_2 shell to simulate the effect of the silica matrix are embedded in an effective medium characterized by a refractive index n_{eff} that is allowed to vary between the refractive indices of SiO_2 and Si . The absorption cross section was calculated assuming the theory of Mie for a spherical particle within the quasi-static approximation:

$$\alpha_A(\omega) = \frac{8\pi^2\sqrt{\varepsilon_m}r^3\omega}{c} Im\left\{\frac{\varepsilon(\omega)-\varepsilon_m}{\varepsilon(\omega)+2\varepsilon_m}\right\}$$

with the dielectric function of heavily doped Si that follows the Drude model :

$$\varepsilon(\omega) = \varepsilon_\infty - \frac{\omega_p^2}{\omega^2 + i\omega\Gamma}$$

where ω_P is the bulk plasma frequency, Γ is the free carrier damping constant (the inverse of the charge carrier scattering time) and ε_∞ is the high frequency dielectric constant of Si-NCs. The bulk plasma frequency ω_P is defined as :

$$\omega_p{}^2 = \frac{n_{Drude} e^2}{m^* \varepsilon_0}$$

where n_{Drude} is the density of free charge carriers, e the electron charge, m^* the effective mass and ε_0 the vacuum permittivity. In the case of a spherical shaped Si-NC subjected to an electromagnetic field and placed in a medium characterized by a dielectric constant ε_m the theory of Mie can be applied and the resonant plasmon frequency can then be written as:

$$\omega_p{}^2 = \frac{n_{Drude} e^2}{m^* \varepsilon_0 (\varepsilon_\infty + 2\varepsilon_m)}$$

The free carrier damping constant Γ, which is defined as :

$$\Gamma = \frac{e}{m^* \mu}$$

is inversely proportional to the charge carrier mobility μ.

Figure 7(b) shows the experimental infrared absorption spectra (red lines) superimposed with the simulated spectra (blue dotted lines calculated using PyMieScatt package) for P-doped multilayers with P concentrations ranging between 0.7 and 1.9 at%. For all the samples, the diameter of the core is maintained equal to 10 nm. In the diameter range explored in this work, i.e. between 5 and 12 nm, no significant modification is observed in the simulation. However in our model, which is able to simulate both vibrational and electronic contributions, the diameter of the shell d_{shell} is a parameter that needs to be adjusted to obtain the correct intensity r)atio between both vibrational and electronic features. The density of free charge carriers

n_{Drude} as well as the charge carrier mobility μ are varied to simulate correctly both the position and the width of the LSPR band. Moreover, the refractive index of the effective medium n_{eff} is varied between the refractive indices of SiO_2 and Si to simulate correctly the position of the vibrational peaks. For all the samples, a good agreement is obtained for $n_{eff}=3$, which suggests that the core-shell nanoparticles feel a surrounding medium that is strongly influenced by the presence of other Si-NCs. The simulated spectra are found to correctly match the experimental spectra for the parameters listed in Table I. The free charge carrier density, which corresponds to the concentration of active P atoms inserted in the Si-NCs, is found to increase from 2×10^{20} cm^{-3} to 2.3×10^{20} cm^{-3} when the P content increases from 0.7 at% to 1.1 at%, i.e. corresponding to P concentrations in the Si-NCs equal to 5.6 at% and 10.3 at%, respectively. Assuming an atomic concentration of Si of 5×10^{22} cm^{-3}, and based on the P atomic concentration given in Fig. 3(c), this corresponds to a P activation rate of 8 and 4.6 %, respectively. In bulk silicon, this value is highly dependent on the doping level and on the annealing treatments carried out to activate dopants. The values obtained in this study are lower than those reported for highly P-doped Si nanodisks, which can reach values as high as 70 %[26]. In the latter, dopants were introduced by low energy implantation of P into bulk Si and the dopant activation was promoted by laser thermal annealing allowing strong out of equilibrium conditions. The activation efficiency reported in this work is, however, significantly larger than the P activation efficiencies reported for free-standing P-doped Si-NCs which is lower than 1 %[24] or for P-doped Si-NCs obtained by diffusion doping of freestanding Si/SiO_x core/shell Si-NCs via high temperature annealing in phosphorus vapor for which the activation efficiency is in the range of 0.8-7 %[38]. In the latter work, this value is underestimated by the presence of inactive P atoms in the oxide shell which give rise to activation efficiency of 34 % after chemical etching of the oxide shell. The value reported here is further in good agreement with activation efficiency values between 3 and 5 % determined for heavily P-doped Si-NCs

embedded in SiO_2[28]. Moreover, the spectral width of the LSPR peak is rather narrow as compared to the values reported in the literature[23,38]. One reason is probably the narrow P concentration distribution of doped Si-NCs, as indicated in Fig. 3(c). Even though we see a heterogeneous broadening of the LSPR peak due to different free carrier concentrations within Si-NCs from one Si-NC to another one, the width of the peak is mainly controlled by the scattering time of free carriers. Based on the simulation, it is then meaningful to extract the charge carrier mobility which is estimated to be around 25 $cm^2V^{-1}s^{-1}$. This value is three times lower than values reported for P-doped bulk Si (i.e. ~ 60 $cm^2V^{-1}s^{-1}$)[39]. The decreased charge carrier mobility could have different origins. According to the recent work of Zhang et al.[28], the size-induced effect on the scattering time may occur for Si-NCs having diameters lower than 5 nm, which is however not the case in our study. It is then rather expected that the weak free charge carrier mobility is induced by the presence of non-active dopants which may generate defects or to small clusters that may act as scattering centers.

4. CONCLUSIONS

To summarize, using P-doped (SiO/SiO_2) multilayers prepared by evaporation, we have shown that P atoms can be inserted in the core of Si-NCs embedded in a silica matrix with concentrations well beyond the solid solubility limit of P in bulk Si. Structural and chemical analysis allowed us to demonstrate that most of P dopants are localized in Si-NCs and the P content in Si-NCs can reach values as high as 10 at%. Infrared absorption measurements gave evidence of a tunable LSPR band induced by the activation of dopants that give rise to free electrons. After subtraction of optical interferences in the thin layer and thanks to a core-shell modeling of Si-NCs embedded in a silica matrix, simulations based on the theory of Mie and the Drude model allowed us to reproduce correctly both the vibrational and the electronic contributions to the absorption spectra. Both the charge carrier mobility and their density were determined. A free carrier concentration as high as 2×10^{20} cm^{-3} corresponding to a doping

efficiency of 8 % was obtained. The charge carrier mobility is estimated to 25 $cm^2V^{-1}s^{-1}$, i.e. between 2 and 3 times lower than the charge carrier mobility in bulk Si. This low carrier mobility can be explained by P atoms that are not electronically active. Our work is the first report on a tunable LSPR in highly doped Si-NCs obtained using the multilayer architecture. It is an interesting and promising method to implement such plasmonic structures in future nanophotonic devices operating in the infrared range.

ACKNOWLEDGMENTS

The authors acknowledge the French PIA project "Lorraine Université d'Excellence", reference no. ANR-15IDEX-04-LUE and the ANR project DONNA (ANR-18-CE09-0034) for support. This work was partially supported by the CNRS Federation IRMA-FR 3095.

References:

(1) Hoffman F. M., Infrared reflection absorption spectroscopy of adsorbed molecules, *Surf. Sci. Rep.* **1983**, *3,* 107-192.

(2) Unser S.; Bruzas I.; He J.; Sagle L. Localized surface plasmon resonance biosensing: current challenges and approaches, *Sensors* **2015**, *15*, 15684-15716.

(3) Comin A.; Manna L. New materials for tunable plasmonic colloidal nanocrystals, *Chem. Soc. Rev.* **2014**, *43*, 3957-3975.

(4) Liu X.; Swihart M. T. Heavily doped colloidal semiconductor and metal oxide nanocrystals: an emerging new class of plasmonic nanomaterials, *Chem. Soc. Rev.* **2014**, *43*, 3908-3920.

(5) Zhong Y.; Malagari S. D.; Hamilton T.; Wassermann D. Review of mid-infrared plasmonic materials, *J. Nanophotonics* **2015**, *9*, 093791.

(6) Soref R.; Peale R. E.; Buchwald W. Longwave plasmonics on doped silicon and silicides, *Optics Express* **2008**, *16*, 6507-6514.

(7) Smith E. M.; Streyer W. H.; Nader N.; Vangala S.; Grzybowski G.; Soref R.; Wasserman D.; Cleary J. W. Metal germanides for practical on-chip plasmonics in the mid infrared, *Optical Materials Express* **2018**, *8*, 968-982.

(8) Naik G. V.; Kim J.; Boltasseva A. Oxides and nitrides as alternative plasmonic materials in the optical range, *Opt. Mat. Express* **2011**, *1*, 1090-1099.

(9) Naik G. V.; Liu J.; Kildishev A. V.; Boltasseva A. Demonstration of Al:ZnO as a plasmonic component for near infrared metamaterials, *Proc. Natl. Acad. Sci. USA* **2012**, *109*, 8834-8838.

(10) Naik G. V.; Schroeder J. L.; Ni X.;Kildishev A. V.; Sands T. D.; Boltasseva A. Titanium nitride as a plasmonic material for visible and near infrared wavelengths, *Opt. Mat. Express* **2012**, *2*, 478-489.

(11) Agrawal A.; Cho S. H.; Zandi O.; Ghosh S.; Johns R. W.; Milliron D. J. Localized surface plasmon resonance in semiconductor nanocrystals, *Chem. Rev.* **2018**, *118*, 3121-3207.

(12) Luther J. M.; Jain P. K.; Ewers T.; Alivisatos A. P. Localized surface plasmon resonances arising from free carriers in doped quantum dots, *Nat. Mater.* **2011**, *10*, 361-366.

(13) Kriegel L.; Jiang C.; Rodriguez-Fernandez J.; Schaller R. D.; Talapin D. V.; Da Como E.; Feldmann J. Tuning the excitonic and plasmonic properties of copper chalcogenide nanocrystals, *J. Am. Chem. Soc.* **2012**, *134*, 1583-1590.

(14) Kriegel L.; Rodriguez-Fernandez J.; Wisnet A.; Zhang H.; Waurisch C.; Eychmüller A.; Dubavik A.; Govorov A. O.; Feldmann J. Shedding light on vacancy doped copper chalcogenides: shape-controlled synthesis, optical properties and modelling of copper telluride nanocrystals with near-infrared plasmon resonances, *ACS Nano* **2013**, *7*, 4367-4377.

(15) Schimpf A. M.; Thakkar N.; Gunthardt C .E.; Masiello D. J.; Gamelin D. R. Charge tunable quantum plasmons in colloidal semiconductor nanocrystals, *ACS Nano* **2014**, *8*, 1065-1072.

(16) Li S. Q.; Guo P.; Zhang L.; Zhou W.; Odom T. W.; Seideman P.; Ketterson J. B.; Chang R. P. H. Infrared plasmonics with indium tin oxide nanorod arrays, *ACS Nano* **2011**, *5*, 9161-9170.

(17) Dalpian G. M.; Chelikowsky J. R. Self-purification in semiconductor nanocrystals, *Phys. Rev. Lett.* **2006**, *96*, 226802.

(18) Khelifi R.; Mathiot D.; Gupta R.; Muller D.; Roussel M.; Duguay S. Efficient n-type doping of Si nanocrystals embedded in SiO_2 by ion beam synthesis, *Appl. Phys. Lett.* **2013**, *102*, 013116.

(19) Gnaser H.; Gutsch S.; Wahl M.; Schiller R.; Kopnarski M.; Hiller D.; Zacharias M. Phosphorus doping of Si nanocrystals embedded in silicon oxynitride determined by atom probe tomography, *J. Appl. Phys.* **2014**, *115*, 034304.

(20) Trad F.; Giba A. E.; Devaux X.; Stoffel M.; Zhigunov D.; Bouché A.; Geiskopf S.; Demoulin R.; Pareige P.; Talbot E.; Vergnat M.; Rinnert H. Influence of phosphorus on the

growth and the photoluminescence properties of Si-NCs formed in P-doped SiO/SiO_2 multilayers, *Nanoscale* **2021**, *13*, 19617-19625.

(21) Pi X.; Delerue C. Tight binding calculations of the optical response of optimally P-doped Si nanocrystals: a model for localized surface plasmon resonance, *Phys. Rev. Lett.* **2013**, *111*, 177402.

(22) Rowe D. J.; Jeong J. S.; Mkhoyan K. A.; Kortshagen U. R. Phosphorus doped Si nanocrystals exhibiting mid-infrared localized surface plasmon resonance, *Nano Lett.* **2013***, 13*, 1317-1322.

(23) Kramer N. J.; Schramke K. S.; Kortshagen U. R. Plasmonic properties of Si nanocrystals doped with boron and phosphorus, *Nano Lett.* **2015***, 15*, 5597-5603.

(24) Zhou S.; Pi X.; Ni Z.; Ding Y.; Jiang Y.; Jin C.; Delerue C.; Yang D.; Nozaki T. Comparative study of the localized surface plasmon resonance of Boron-and Phosphorus doped Si nanocrystals, *ACS Nano* **2015**, *9*, 378-386.

(25) Zhang H.; Zhang R.; Schramke K. S.; Bedford N. M.; Hunter K.; Kortshagen U. R.; Nordlander P. R., Doped silicon nanocrystal plasmonics, *ACS Photonics* **2017***, 4*, 963-970.

(26) Poumirol J. M.; Majorel C.; Chery N.; Girard C.; Wiecha P. R.; Mallet N.; Monflier R.; Larrieu G.; Cristiano F.; Royet A. S.; Acosta-Alba P.; Kerdilès S.; Paillard V.; Bonafos C. Hyper-doped silicon nanoantennas and metasurfaces for tunable infrared plasmonics, *ACS Photonics* **2021***, 8*, 1393-1399.

(27) Majorel C.; Paillard V.; Patoux A.; Wiecha P. R.; Cuche A.; Arbouet A.; Bonafos C.; Girard C. Theory of plasmonic properties of hyper-doped silicon nanostructures, *Optics Communications* **2019***, 453*, 124336.

(28) Zhang M.; Poumirol J. M.; Chery N.; Majorel C.; Demoulin R.; Talbot E.; Rinnert H.; Girard C.; Cristiano F.; Wiecha P. R.; Hungria T.; Paillard V.; Arbouet A.; Pécassou B.;

Gourbilleau F.; Bonafos C. Infrared nanoplasmonic properties of hyperdoped embedded Si nanocrystals in the few electrons regime, *Nanophotonics* **2022**, *11*, 3485-3493.

(29) Zacharias M.; Heitmann J.; Scholz R.; Kahler U.; Schmidt M.; Blasing J. Size-controlled highly luminescent Si nanocrystals: a SiO/SiO_2 superlattice approach, *Appl. Phys. Lett.* **2002**, *80*, 661-663.

(30) Jambois O.; Rinnert H.; Devaux X.; Vergnat M. Photoluminescence and electroluminescence of size-controlled Si nanocrystallites embedded in SiO_2 thin films, *J. Appl. Phys.* **2005**, *98*, 046105.

(31) Lippert G.; Osten H. J.; Krüger D.; Gaworzewski P.; Eberl K. Heavy phosphorus doping in molecular beam epitaxial grown silicon by a GaP decomposition source, *Appl. Phys. Lett.* **1995***, 66*, 3197-3199.

(32) Geiskopf S.; Stoffel M.; Devaux X.; André E.; Carteret C.; Bouché A.; Vergnat M.; Rinnert H. Formation of SiP_2 nanocrystals embedded in SiO_2 from phosphorus-rich $SiO_{1,5}$ thin films, *J. Phys. Chem. C* **2020**, *124*, 7973-7978.

(33) Geiskopf S.; Valdenaire A.; Stoffel M.; Devaux X.; André E.; Carteret C.; Bouché A.; Vergnat M.; Rinnert H. Thin films of SiP lamellar alloys: a first step toward 2D SiP, *J. Phys. Chem. C* **2021**, *125*, 3235-3241.

(34) Hao X. J.; Cho E.-C.; Scardera G.; Bellet-Amalric E.; Bellet D.; Shen Y. S.; Huang S.; Huang Y. D.; Conibeer G.; Green M. A. Effects of Phosphorus Doping on Structural and Optical Properties of Silicon Nanocrystals in a SiO_2 Matrix, *Thin Solid Films* **2009**, *517*, 5646−5652.

(35) Demoulin R.; Roussel M.; Duguay S.; Muller D.; Mathiot D.; Pareige P.; Talbot E. Atomic scale characterization of N-doped Si nanocrystals embedded in SiO_2 by atom probe tomography, *J. Phys. Chem. C* **2019**, *123*, 7381-7389.

(36) Pai P. G.; Chao S. S.; Takagi Y. Infrared spectroscopy study of SiO_x thin films produced by plasma enhanced chemical vapor deposition, *J. Vac. Sci. Technol A* **1986**, *4*, 689-694.

(37) Swanepoel R. Determination of the thickness and optical constants of amorphous silicon, *J. Phys. E: Sci. Instrum*. **1983***, 16*, 1214-1222.

(38) Bubenov S. S.; Dorofeev S. G.; Eliseev A. A.; Kononov N. N.; Gershev A. V.; Mordvinova N. E.; Lebedev O. I. Diffusion doping route to plasmonic Si/SiO_x nanoparticles, *RSC Advances* **2018**, *8*, 18896-18903.

(39) Masetti G.; Severi M.; Solmi S. Modeling of carrier mobility against carrier concentration in Arsenic, Phosphorus and Boron doped silicon, *IEEE Trans. El. Dev.* **1983**, *ED 30*, 764-769.

Figure captions

Scheme 1: P-doped (SiO/SiO_2) multilayer structure grown on a Si(001) substrate prior to and after annealing at 1100°C for 15 minutes under N_2 flow (200 sccm). The annealing destabilizes the SiO layer thus leading to the formation of Si nanocrystals embedded in a SiO_2 matrix.

Figure 1: Chemical composition of the P-doped SiO/SiO_2 multilayers as a function of the temperature of the GaP decomposition source.

Figure 2: Transmission electron microscopy analysis of a P-doped SiO/SiO_2 multilayer with a P content of 1.1 at%. (a) EFTEM image taken at an energy of 25 eV (1 eV range) highlighting the SiO_2 matrix, (b) HRTEM image of a single doped Si nanocrystal embedded in the silica matrix. The inset shows a fast Fourier transform (FFT) of the HRTEM image. Quantitative chemical maps extracted from the processing of an EELS spectrum image for Si^0 (c), P(d) and Si^{IV} present in SiO_2 (e), (f) Histograms of the Si-NC size distributions for both undoped and doped SiO/SiO_2 multilayers with the P content varying between 0.7 at% and 1.9 at% .

Figure 3: (a)-(b) 2D slice views (46 x 46 x 10 nm^3) taken from the 3D reconstructed volume showing both Si atoms (red points) and phosphorus atoms (black points) for the P-doped SiO/SiO_2 multilayer containing 1.1 at% of P. (c) P concentration in the Si-NCs as a function of their diameter for P-doped SiO/SiO_2 multilayers containing 0.7 and 1.1 at% of P.

Figure 4: (a) STEM-HAADF image of a P-doped SiO/SiO_2 multilayer containing 4,1 at% of P. The Si substrate is identified on the left of the image. (b) EDS spectra taken in the SiO_2 matrix (blue solid line) and in a nanoparticle (red solid line). In the nanoparticles, SiP is identified assuming that all detected oxygen originates from the SiO_2 matrix.

Figure 5: (a) Evolution of the PL spectra measured at RT on an undoped SiO/SiO_2 multilayer prior to and after annealing at various temperatures between 950°C and 1100°C for 5 minutes. The PL spectrum obtained after annealing at 1100°C for 15 minutes is also shown.(b) Evolution of the PL spectra measured at RT for P-doped SiO/SiO_2 multilayers with different P contents ranging between 0 (undoped) and 4.1 at% of P after annealing at 1100°C for 15 minutes.

Figure 6: (a) Infrared absorption spectrum measured for the P-doped SiO/SiO_2 multilayer containing 1.1 at% of P (black solid line). The background simulated using the model of Swanepoel is shown as a red solid line. (b) Evolution of the infrared absorption spectra measured on P-doped SiO/SiO_2 multilayers with the P content varying between 0 and 4.1 at% after background subtraction. The evolution of the band close to 2000 cm^{-1} is highlighted in the inset.

Figure 7: (a) Scheme of the core-shell model used for the simulations, (b) Experimental infrared absorption spectra (red solid lines) and simulated spectra (blue dotted lines) for P-doped SiO/SiO_2 multilayers containing 0.7 at% of P, 1.1 at% of P and 1.9 at% of P. The insets highlight the experimental and simulated LSPR band close to 2000 cm^{-1}.

Table I: Free carrier density and mobility obtained from the simulations for different P contents

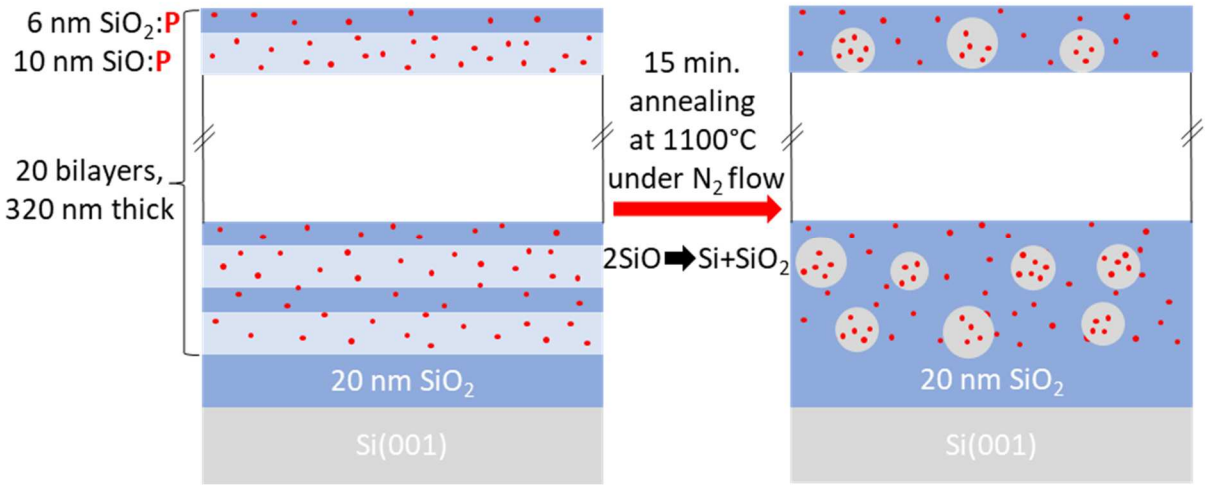
6 nm SiO2:P
10 nm SiO:P
20 bilayers,
320 nm thick
20 nm SiO2
Si(001)
15 min.
annealing
at 1100°C
under N2 flow
2SiO➡Si+SiO2
20 nm SiO2
Si(001)

Scheme 1

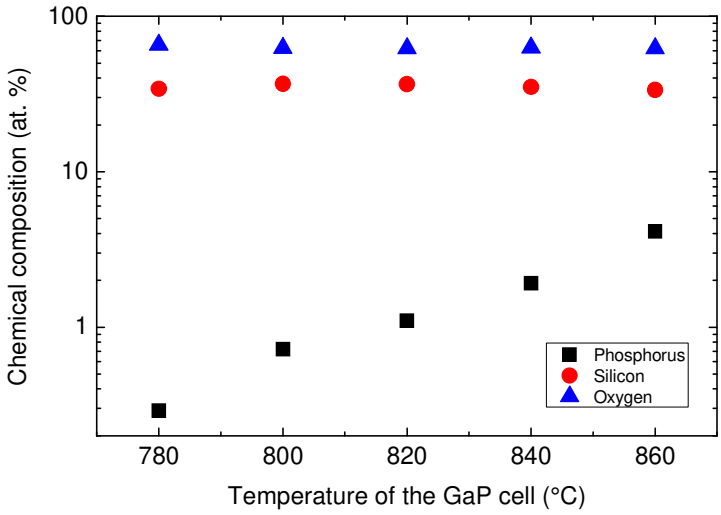
100
10
1
Chemical composition (at. %)
780
800
820
840
860
Temperature of the GaP cell (°C)
Phosphorus
Silicon
Oxygen

Figure 1

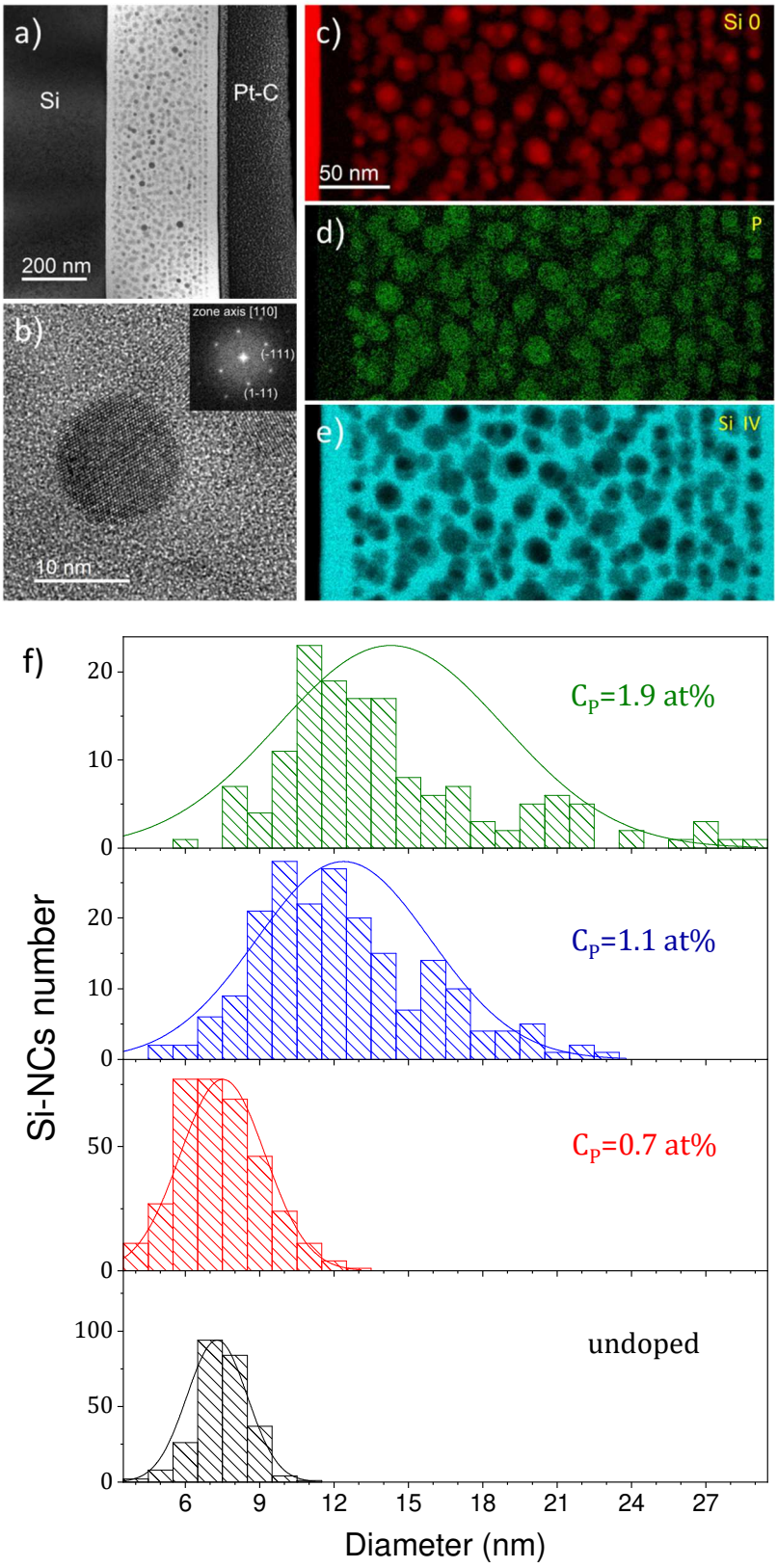
a)
Si
Pt-C
200 nm
b)
zone axis [110]
(-111)
(1-11)
10 nm
c)
Si 0
50 nm
d)
P
e)
Si IV
f)
Si-NCs number
C_P=1.9 at%
C_P=1.1 at%
C_P=0.7 at%
undoped
Diameter (nm)

Figure 2

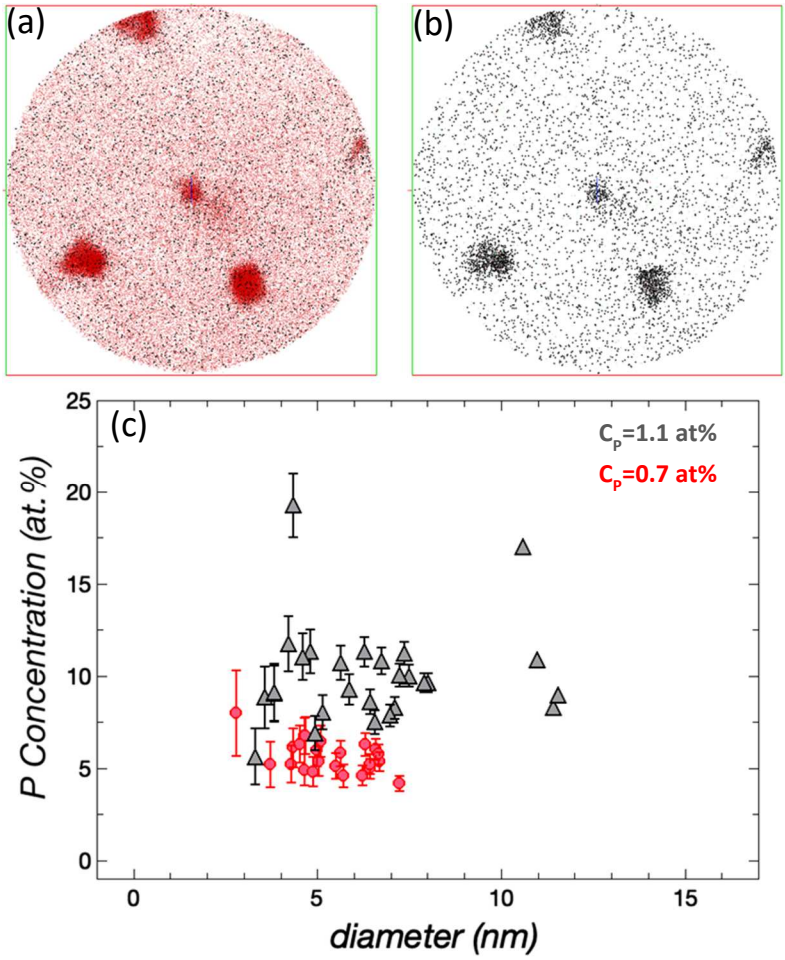
(a)
(b)
(c)
C_P=1.1 at%
C_P=0.7 at%
P Concentration (at.%)
diameter (nm)
0
5
10
15
20
25

Figure 3

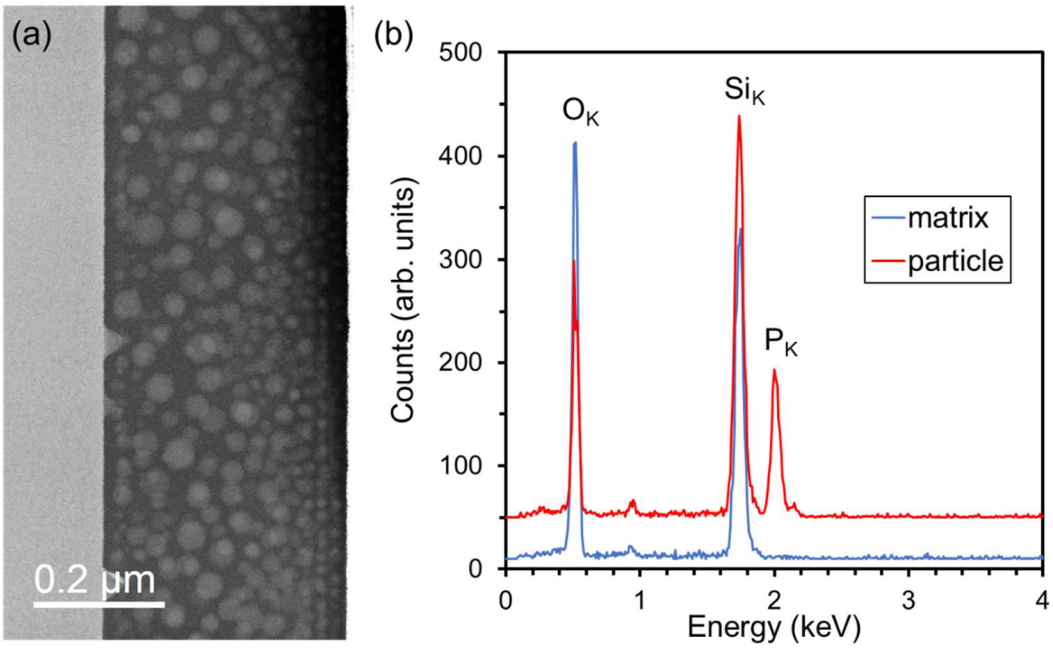
(a)
0.2 μm
(b)
500
400
300
200
100
0
Counts (arb. units)
O_K
Si_K
P_K
matrix
particle
0
1
2
3
4
Energy (keV)

Figure 4

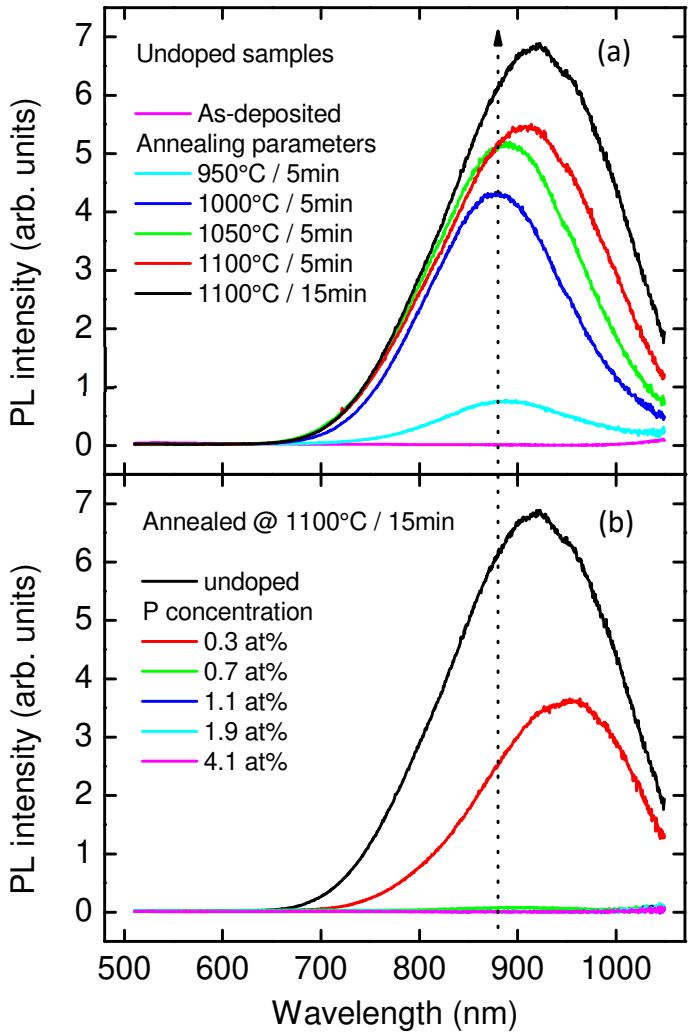
Undoped samples
(a)
As-deposited
Annealing parameters
950°C / 5min
1000°C / 5min
1050°C / 5min
1100°C / 5min
1100°C / 15min
PL intensity (arb. units)
Annealed @ 1100°C / 15min
(b)
undoped
P concentration
0.3 at%
0.7 at%
1.1 at%
1.9 at%
4.1 at%
PL intensity (arb. units)
Wavelength (nm)

Figure 5

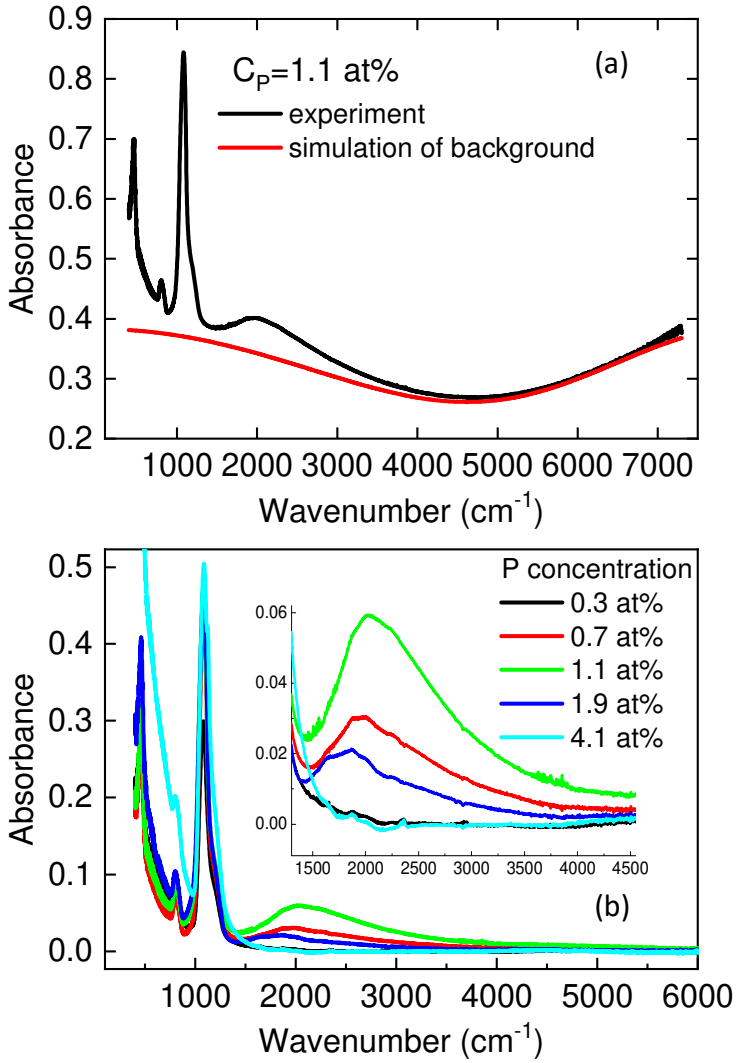
0.9
0.8
0.7
0.6
0.5
0.4
0.3
0.2
Absorbance
C_P=1.1 at%
(a)
experiment
simulation of background
1000 2000 3000 4000 5000 6000 7000
Wavenumber (cm^{-1})
0.5
0.4
0.3
0.2
0.1
0.0
Absorbance
P concentration
0.3 at%
0.7 at%
1.1 at%
1.9 at%
4.1 at%
0.06
0.04
0.02
0.00
1500 2000 2500 3000 3500 4000 4500
(b)
1000 2000 3000 4000 5000 6000
Wavenumber (cm^{-1})

Figure 6

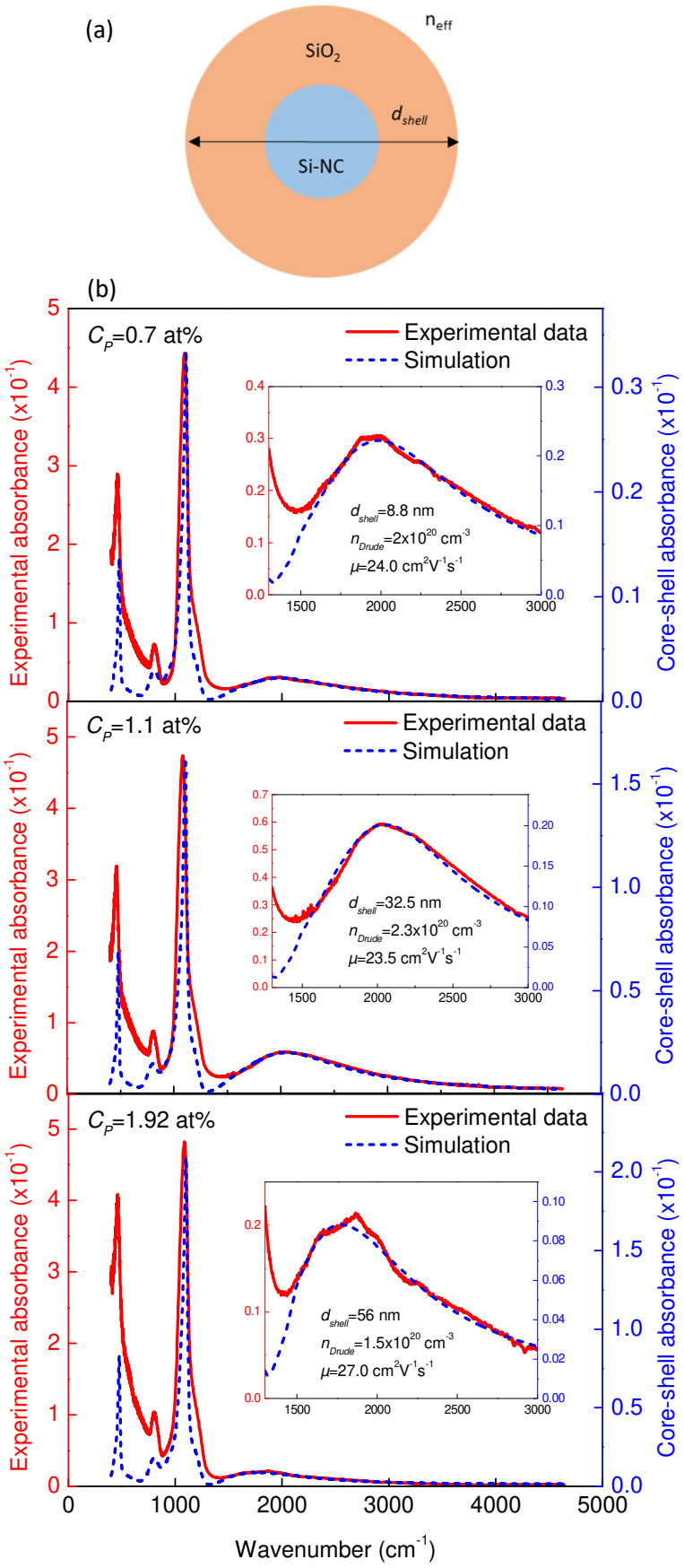
(a)
n_{eff}
SiO_2
d_{shell}
Si-NC
(b)
C_P=0.7 at%
Experimental data
Simulation
d_{shell}=8.8 nm
n_{Drude}=2x10^{20} cm^{-3}
μ=24.0 cm^{2}V^{-1}s^{-1}
C_P=1.1 at%
Experimental data
Simulation
d_{shell}=32.5 nm
n_{Drude}=2.3x10^{20} cm^{-3}
μ=23.5 cm^{2}V^{-1}s^{-1}
C_P=1.92 at%
Experimental data
Simulation
d_{shell}=56 nm
n_{Drude}=1.5x10^{20} cm^{-3}
μ=27.0 cm^{2}V^{-1}s^{-1}
Experimental absorbance (x10^{-1})
Core-shell absorbance (x10^{-1})
Wavenumber (cm^{-1})

Figure 7

at% P	Tcel (°C)	Free carrier density (cm^{-3})	Mobility ($cm^2 s^{-1} V^{-1}$)
0.7	800	$2\ 10^{20}$	24
1.1	820	2.3×10^{20}	25
1.9	840	1.5×10^{20}	28

Table I